

phaser: An all-in-one package for (multislice) electron ptychography

Colin Gilgenbach¹ and James M. LeBeau^{1,*}

¹*Massachusetts Institute of Technology*

(Dated: June 11, 2025)

Electron ptychography is a groundbreaking technique for the advanced characterization of materials. Successful ptychography relies on robust implementations of reconstruction algorithms with process raw data into phase images. Current software has enabled deep sub-angstrom multislice electron ptychographic reconstructions, but reconstructions remain challenging and computationally expensive. In addition, current software generally lacks the modularity to act as a platform for the development and testing of new solver components and algorithms. For instance, algorithms based on gradient descent and autodifferentiation promise faster reconstructions with higher quality, but it is difficult to implement these algorithms in existing software. Here, we present **phaser**, an open source Python package which provides a unified interface to both conventional and gradient descent based ptychographic algorithms. Reconstructions are specified in a declarative format, and can be run from a command line, Jupyter notebook, or web interface. Multiple computational backends are supported to provide maximum flexibility. With the JAX computational backend, a 6x improvement in iteration speed is achieved over a state-of-the-art package, `fold.slice`. Additionally, **phaser**'s gradient descent solver achieves improved reconstruction quality.

I. Introduction

Electron ptychography is emerging as an important technique for the advanced characterization of materials. In STEM, ptychography has been used to image materials with record-breaking, deep sub-angstrom resolution [1–5]. Moreover, as a phase contrast technique, ptychography provides information of both heavy and light elements, and multislice ptychography provides 3D information beyond the diffraction limit [6–10].

As a computational imaging technique, the algorithms to reconstruct ptychographic data are as critical as the experiment which collects the data. Thus, the development of ptychography as an experimental technique runs parallel to the development of ptychographic reconstruction algorithms. The first prominent algorithm for ptychographic reconstruction was Wigner Distribution Deconvolution (WDD) [11]. This algorithm deconvolves the 4D dataset into two Wigner functions, one corresponding to the probe and one corresponding to the object. This technique is shown to be relatively robust to noise and to partial coherence, but has the disadvantage of being computationally expensive.

The development of iterative algorithms for ptychography such as PIE and ePIE [12, 13] was a key breakthrough. These algorithms progress probe position-by-probe position, applying a forward simulation and then updating estimates of the object function using the mismatch between the forward simulated and experimental data. The ePIE algorithm has been applied to ptychography in X-ray [14], SEM [15], and STEM [1, 16, 17].

With iterative algorithms, more accurate forward models achieve better reconstructions. For instance, the ePIE algorithm relies on the strong phase object approximation (SPOA), which does not apply for STEM samples thicker than a few nm. Multislice ptychography [18, 19] replaces the single slice forward model of ePIE with the multislice model [20], enabling the imaging of thick samples which exhibit dynamical scattering. Another improvement is mixed state ptychography [21], which models the probe and/or object as a weighted sum of mutually incoherent waves. In STEM, a mixed state probe is critical to model partial spatial coherence, which in STEM is on the order of the electron probe's diffraction limit ($\sim 0.5 \text{ \AA}$) [22].

Beyond improved forward models, advanced gradient update methods can be used as in the maximum-likelihood algorithm [23, 24]. Additionally, the choice of loss function allows the noise statistics of the experiment to be accounted for [23, 25]. Alternatively, the iterative problem can be framed as a constraint satisfaction problem, and solved with algorithms such as the difference map [26, 27]. Together, these algorithmic improvements have enabled deep sub-angstrom resolution in electron ptychography [2, 3].

Recently, there has been a focus on ptychographic reconstructions performed with gradient descent (sometimes referred to as “Wirtinger flow”) and often implemented via autodifferentiation software [28–34]. Framing the ptychographic problem this way allows easy implementation of new forward models and reconstruction variables, as the gradient step can be calculated automatically from the forward model.

A wide range of software packages have been developed for ptychography [32, 34–38]. However, there is still a need for software which acts as a

* lebeau@mit.edu

platform for developing next-generation algorithms for multislice electron ptychography, without compromising performance or ease-of-use by users at all experience and programming skill levels.

Here, we present **phaser**, an open-source python package for performing ptychographic reconstructions. **phaser** provides a unified interface for both conventional ptychography algorithms (ePIE and LSQML) as well as gradient-descent-based ptychographic reconstruction algorithms. **phaser** is designed to support multiple incoherent probe modes and multi-slice ptychography, and is designed to be robust to experimental data. A modular architecture provides flexibility in the reconstruction process while retaining speed and ease of use. A client-server architecture allows scaling computation from a single computer to clusters and high performance computing, and allows the immediate visualization of reconstruction results.

II. Software architecture

A key challenge in software design is the balance between the flexibility of the interface, the ease of coding, and the resulting ease of use. **phaser** attempts to avoid this compromise through the use of ‘hooks’, which allow the specification of reconstruction plans in a modular format. Hooks take the form of functions that implement an abstract interface. The hooks are called by the main reconstruction algorithm to provide extensible points of customization. Hooks can be specified in the reconstruction plan file and can take parameters specified by the user as well as arguments passed by the software. Hooks may be provided with the default distribution or can be coded by an advanced user. As an example, a hook is used to implement the detector noise model in reconstruction. The end user can choose one of the built-in noise models (Gaussian, amplitude, Poisson, etc.), or provide their custom noise model as a Python function. At the same time, solvers share a common interface for noise models, so a noise model implemented for one solver can be used in any other solver. The use of hooks allows the core software package to remain simple while retaining flexibility for the advanced user, and the configurability of hooks allows even the novice user to take advantage of them.

Reconstructions in **phaser** are specified through ‘plans’, which are a declarative description of the reconstruction process to perform. Plans may be instantiated in Python code or specified through a YAML or JSON interface. Reconstruction plans are parsed and validated prior to reconstruction using the **pane** library, giving the user quick feedback on invalid parameters. Since plans are specified in a declarative format, they may be generated by other code (such as a hyperoptimization framework or a microscope macro) and easily transmitted over the web to remote workers. The reconstruction plan schema is versioned, and allows the specification of

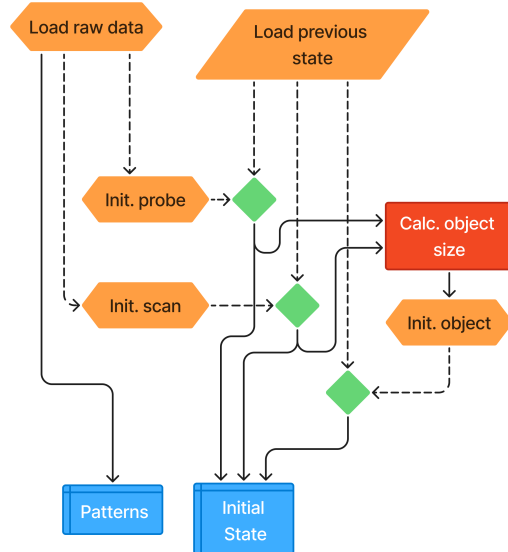


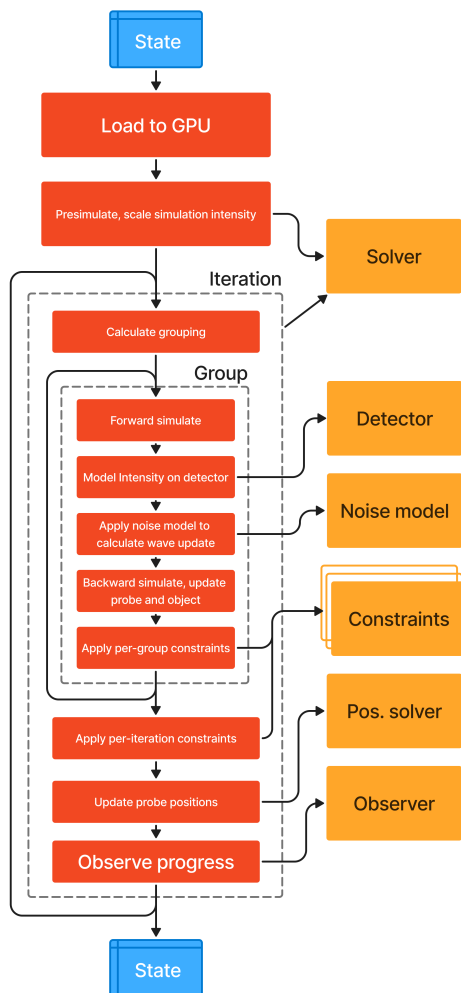
Figure 1. Data-loading and initialization workflow used at the start of each reconstruction to initialize reconstruction state. Solid arrows indicate mandatory data dependencies, while dashed arrows indicate optional dependencies. Yellow boxes indicate reconstruction ‘hooks’ where behavior can be customized. The raw data hook is responsible for loading diffraction patterns, and can optionally provide information about the initial probe and scan. Previous reconstruction state may be provided with another hook. In this case, data from the previous reconstruction is combined (green diamonds) with newly initialized data to create the initial reconstruction state. Total object size is calculated as a function of the scan and probe extent, and is passed to the object initialization hook.

hooks both built-in and third-party. These features help make ptychographic reconstructions more reproducible, especially in scientific publications.

The data loading and simulation initialization process of **phaser** is schematically outlined in Figure 1, where hooks are specified by yellow boxes and lines indicate data dependencies. When a plan is executed, first the raw data is loaded from a hook (which implements detector-specific I/O). Optionally, the raw data hook may supply metadata about the probe and scan (e.g. a focused probe and raster scan). This information, optionally with the previous reconstruction state, is used to produce two outputs: a set of loaded diffraction patterns and an initial reconstruction state. These outputs are then passed through reconstruction ‘engines’ in sequence.

After data loading, each reconstruction engine is executed in turn. Prior to each engine, reconstruction state is resampled to conform with the engine reconstruction parameters. This includes padding/cropping/resampling the probe, diffraction

Conventional Engine



Gradient Engine

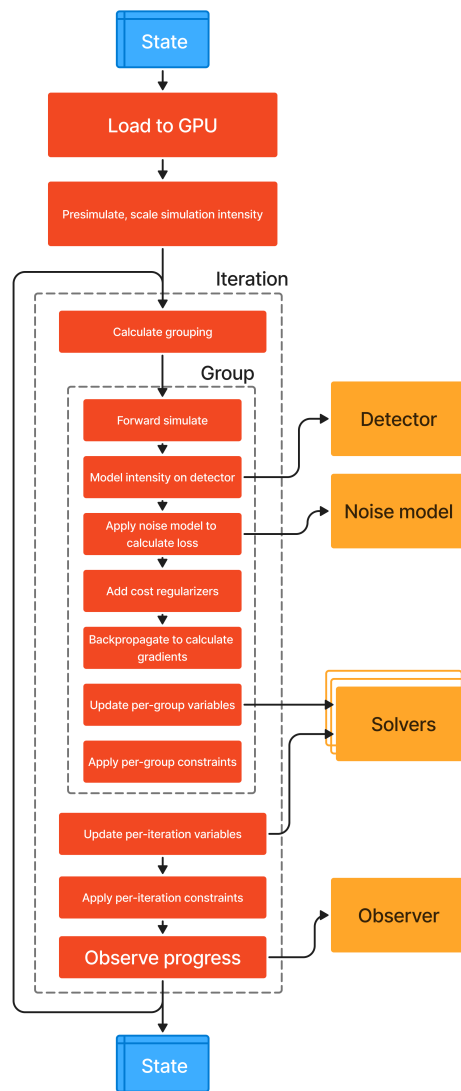


Figure 2. Flowchart of engine operation. Left shows conventional engine workflow, right shows the gradient descent engine. Both engines begin by loading a stored state to the GPU and presimulating the expected diffraction intensity (red blocks). Each reconstruction iteration (black dashed frame) is subdivided into groups of diffraction patterns. For each group, a forward simulation is performed, the noise model is applied, and variables updated. Per-group constraints are also applied. After all groups are processed, iteration-level variables are updated, additional constraints are applied, and progress metrics are sent to observers. Several components are implemented through modular hooks (yellow boxes), which can be replaced by the end user to modify functionality. This decoupled design allows rapid experimentation with alternative loss functions, optimizers, and regularization strategies while preserving the proven scheduling and monitoring infrastructure.

patterns, and object, as well as resampling the object slices in Z and increasing/decreasing the number of probe modes. The flow of the two main engines implemented in `phaser`—the conventional engine and the gradient descent engine are indicated in Figure 2. Each engine consists of solvers—hooks which implement the specify reconstruction algorithms. Both engines begin by loading the data to the GPU, followed by a precalculation

step. This is used to initialize variables needed in the reconstruction, such as the object magnitude and probe magnitude, as well as to ensure that probe intensity matches with the intensity of the experimental data. Each engine operates on a subset (called a ‘group’) of probe positions at once. This group may be chosen from a sparse or a compact grouping of the overall probe positions. By default, this grouping is randomized per

iteration of the solver, and the order in which groups are updated is shuffled in each iteration. This is in accordance with standard practice in deep learning [39]. In both engines, the forward model is simulated, which results in a modeled intensity on the detector. This involves the cutout of individual sub-regions of the shared object, the independent propagation of each probe mode through the sample, and the resampling of the exit wavefield onto the detector. In the conventional engine, the wavefront is updated to calculate a wavefront update, χ , which is propagated back to the exit plane of the sample. At each slice in the object, this wavefront update is used to calculate an object update, as well as an update to the entry wavefront at that slice. This entry wavefront update is propagated backwards to become the wavefront update of the previous slice. Finally, at the entry plane of the object, the probe and probe positions are updated using the final wavefront update. As the wavefront update is modified at every slice, the probe and object updates no longer point in the direction of steepest descent.

In the gradient descent update, after the signal is resampled onto the detector plane, the noise model is applied to calculate a loss function which represents the number of electrons that are misplaced on the detector. Added to this loss function are extra regularizer terms, which act to stabilize the object and probe. Auto-differentiation, implemented by JAX [40], is used to take the gradient with respect to the variables of the simulation. Steps in each of the reconstruction variables are taken as specified by solvers. Hyperparameter schedules can be specified for these solvers. As the gradient calculated from a subset of the probe positions is an estimate of the total gradient (considering all probe positions), this update method is a form of stochastic gradient descent—which has been shown to yield better convergence when training neural networks [41] and when performing phase retrieval [24, 42].

phaser supports being run from the command line or being run from an HTML web interface. When run from the command line, a reconstruction plan file is passed to the **phaser run** sub-command, which performs a single reconstruction in batch mode. The architecture of the worker-server interface is outlined in Figure 3. The server web interface is started with the **phaser serve** sub-command. Using the web interface, ‘workers’ can be started which connect to the server to request reconstruction jobs to run. Workers can run in a separate process on the local computer, run on a remote computer, run on a supercomputing environment or in the cloud. Workers poll the server over HTTP to receive jobs to run. The server has two main functions. The first is to act as a job queue; clients append jobs to this queue to schedule reconstructions, while workers poll the server to request jobs from the queue. The second main function of the server is as a publisher/subscriber (pub/sub) server; workers communicate updates on the

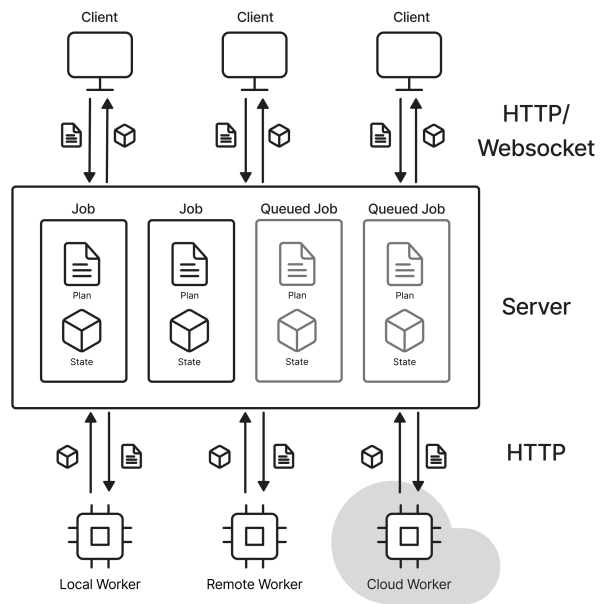


Figure 3. Schematic of server operation of **phaser**. At the center is a server, which serves as a job queue to schedule jobs given by clients (top) to workers (bottom), located locally, remotely, or on the cloud. Reconstruction state is returned by workers to the server, which caches the updated data and publishes to client subscribers. Client-server communications take place over HTTP/Websocket transport, while server-worker communications take place over HTTP with polling.

reconstruction to the server, which caches the current reconstruction state in memory and distributes updates to clients, allowing the live viewing of reconstructions. Communication between the workers and the server takes place over HTTP. Communication between the client and the servers takes place over HTTP/WebSocket transport, which allows for live two-way communication.

phaser can also be run from a Jupyter notebook environment. In this case, the server and the client interface appear as widgets in the Jupyter environment, and can be run locally or remotely. Jobs can be scheduled from the notebook to worker processes, and update can be handled by custom code in the notebook. The notebook environment also provides a convenient interface to view the quality of raw data and experimental parameter selection. **phaser** implements several Jupyter widgets which allow visualization of raw data, acquisition parameters, and reconstructed state. For example, widgets are implemented to show individual convergent-beam electron diffraction (CBED) patterns, position-averaged (PACBED) patterns [46], and virtual detector images. Widgets also allow the visualization of important acquisition parameters in ptychography, including the fundamental ptychographic sampling [43], probe overlap in a single scan position and summed across the scan [45], probe sampling, and the Ronchigram magnification [44]. Reconstructed probes can be viewed in real and

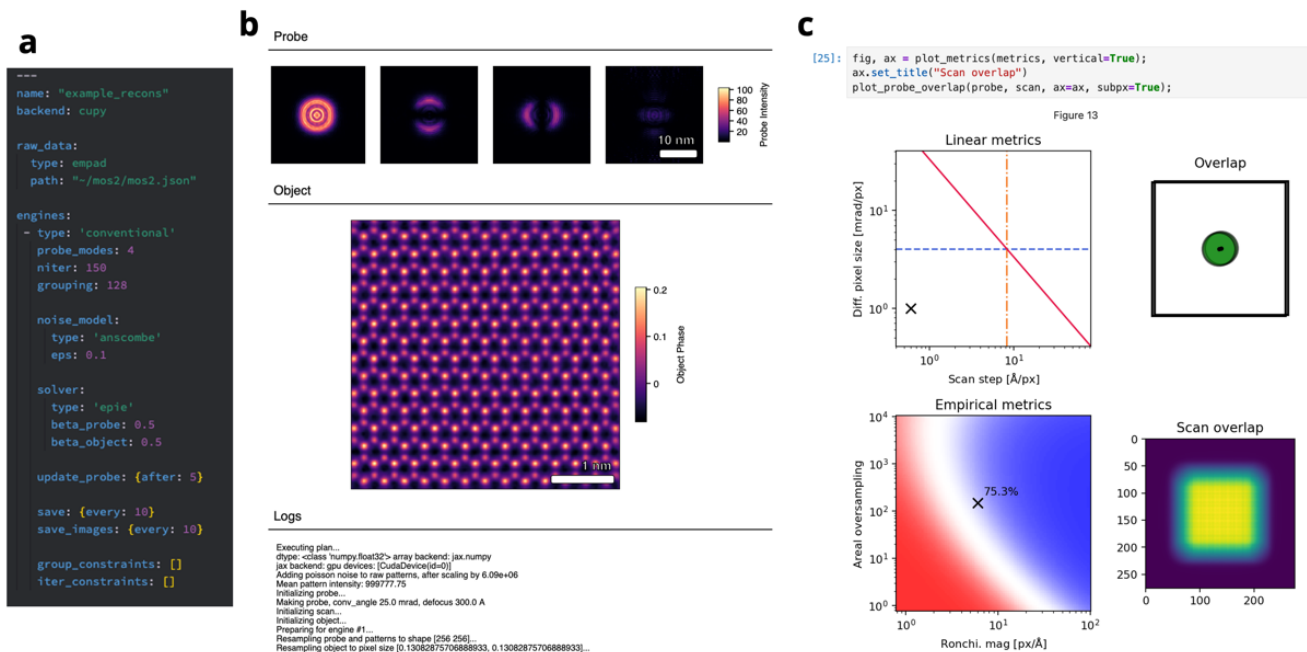


Figure 4. a) Example reconstruction plan file for single slice ptychography with the ePIE engine. Reconstruction plans are specified as declarative YAML files. b) Web interface allowing for remote job submission and live viewing of reconstruction process. Probe and object phase are visible as reconstruction proceeds, as well as log messages and errors from the reconstruction. c) Notebook interface, which provides utilities for viewing raw reconstruction data and analyzing its quality. The plots shown display the dataset’s acquisition parameters with reference to the fundamental ptychographic sampling [43], linear oversampling, probe sampling, areal oversampling, and Ronchigram magnification [44], and provide a view of probe overlap for two scan positions and the entire scan [45].

reciprocal space, and reconstructed objects can be viewed in two and three dimensions.

phaser may be coupled to hyperparameter optimization frameworks, which allow for the optimization of experimental and reconstruction parameters in ptychography [47]. We have experimented using **phaser** with Optuna [48], which implements several optimization algorithms including Bayesian optimization with Gaussian processes (BO-GP) and the tree-structured Parzen estimator (TPE) [49], as well as supporting multi-objective optimization. A variety of error metrics may be used for optimization. When an object ground truth is available, we have found mean-squared error (MSE) to exhibit better performance than structural similarity (SSIM) [50, 51]. Fourier ring correlation (FRC) may be used as well. In the absence of ground truth, the problem is more challenging, as any metric must distinguish between signal and noise, and cannot assume that noise is independently sampled between object pixels. For this reason, the single-image ‘self-FRC’ is often invalid in the setting of ptychography [52].

To provide compatibility across a range of operating systems, accelerators, and environments, **phaser** supports multiple computational backends. Currently, the supported backends are `numpy` [53], `cupy` [54],

and `JAX` [40]. A set of common abstractions are implemented with each of these libraries, and tests ensure identical behavior. This allows **phaser** to operate on Windows, MacOS, and Linux, with CPU, GPU, and tensor-processing unit (TPU) accelerators. **phaser** supports both single- and double-precision calculations, defaulting to single precision. In the future, reduced-precision calculations (e.g. 8- or 16-bit floating point numbers) will be explored to provide speedups, especially in the initial stages of reconstruction. This has been demonstrated in the training and inference of neural networks, where reduced precision reduces both compute and memory bandwidth requirements [55, 56]. Additionally, next-generation accelerators developed for artificial intelligence may prioritize lower precision computations [57].

III. Algorithm description

Ptychography is an inverse problem where, given a series of diffraction patterns taken under shifted illumination, the experimental conditions are found which are ‘most likely’ to yield those diffraction patterns. These diffraction patterns are most often collected on a pixelated camera, but can also be collected with a segmented detector.

Three critical variables contribute to the diffraction patterns measured in ptychography:

- The ‘probe’ P , a complex field variable indicating the amplitude and phase of the incident wavefunction. In the case of mixed-state ptychography, a set of mutually incoherent ‘probe modes’ P_k is used.
- The ‘object’ O , which imparts a phase shift and attenuation (amplitude) to the wavefunction. The object can be two dimensional (single slice) or three dimensional, in which case slices are separated by gaps of thickness Δz_i . In electron microscopy, the object slices are sometimes referred to as “transmission functions”.
- Probe positions X_j . For each position, the probe is shifted to that location and a diffraction pattern taken.

The relevant forward model is the multislice method, which is capable of modeling interaction with a thick specimen as well as multiple scattering. Given a set of probe modes P_k , a 3D object O_i , and a probe position P_j , the wavefunction at each slice is iteratively calculated given the wavefunction at the slice before:

$$\begin{aligned}\Psi_{0,k}(\vec{r}) &= P_k(\vec{r} - X_j) \\ \Psi_{i+1,k}(\vec{r}) &= (\Psi_{i,k}(\vec{r}) \cdot O_i(\vec{r})) * p(\Delta z_i)\end{aligned}$$

In the above, $p(\Delta z)$ indicates a Fresnel free-space propagation kernel of distance Δz , which is convolved with the wavefunction. A bandwidth limit is also applied at this step to prevent aliasing in frequency space [58]. This bandwidth limit is customizable, which is particularly useful for unpadded reconstructions where the Nyquist limit can be relatively small in comparison to traditional multislice simulations.

Finally, given the exit wavefunction $\Psi_{n,k}$, the final intensity in reciprocal space may be calculated:

$$I(\vec{k}) = \sum_k \left| \mathcal{F}(\Psi_{n,k})(\vec{k}) \right|^2$$

The inverse problem consists of taking measured diffraction patterns I_{exp} and recovering the probe P and object O . In the case of single-slice ptychography (where the object is 2D), and the probe positions P_j are perfectly known (and do not fall onto a perfect raster grid), the solution is unambiguous up to a scaling factor of intensity and an affine phase ramp of the object [59]. In practice, the probe positions P_j are not known perfectly, and initial estimates are updated as the algorithm proceeds. This can introduce additional ambiguity, as

in the geometrical optics limit, a change in first order aberrations is equivalent to a linear transformation of the probe positions.

A. Noise models

Ptychography is an overdetermined nonlinear inverse problem. Because the problem is overdetermined, the vast majority of experimental data has no exact solution; any experimental noise whatsoever will likely perturb the problem into this region. This is overcome by the use of maximum likelihood estimation; rather than attempting to find an exact solution, a solution is found which is ‘most likely’ to generate the recorded data given some model of the experimental noise.

The choice of noise model in ptychography has been well-covered in the literature [19,12,18]. Given a modeled intensity $I(\vec{k})$ and a measured intensity $I_{exp}(\vec{k})$, the ideal solution is one which maximizes the probability $P(I|I_{exp})$, i.e the most likely intensity given the experimental data. This is known as the maximum *a posteriori* estimate. This probability can be obtained using Bayes’ theorem:

$$P(I|I_{exp}) = \frac{P(I_{exp}|I)P(I)}{P(I_{exp})}$$

However, usually a good estimate of the prior probabilities $P(I)$ is not known. Using a uniform prior distribution of $P(I)$, maximizing $P(I|I_{exp})$ is equivalent to maximizing the ‘likelihood’ $P(I_{exp}|I)$:

$$\max_I P(I_{exp}|I) = \max_I \prod_{\vec{k}} P(I(\vec{k})|I_{exp}(\vec{k}))$$

In the case of Gaussian noise of variance σ^2 the likelihood is:

$$\begin{aligned}P(I|I_{exp}) &= \prod_{\vec{k}} \frac{1}{\sigma\sqrt{2\pi}} \exp \frac{-(I(\vec{k}) - I_{exp}(\vec{k}))^2}{2\sigma^2} \\ \mathcal{L}(I) &= -\log P(I|I_{exp}) \\ \mathcal{L}(I) &= \sum_{\vec{k}} \frac{1}{2\sigma^2} \left(I(\vec{k}) - I_{exp}(\vec{k}) \right)^2 + \log \left(\sigma\sqrt{2\pi} \right)\end{aligned}$$

As is customary, the loss function $\mathcal{L}(I)$ is defined as the negative log-likelihood. The second term above is a normalization constant and can be ignored. In the case of Poisson noise, variance is not constant, but scales with mean intensity.

The likelihood is:

$$P(I|I_{exp}) = \prod_{\vec{k}} \frac{I(\vec{k})^{I_{exp}(\vec{k})} e^{-I(\vec{k})}}{I_{exp}(\vec{k})!}$$

$$\mathcal{L}(I) = \sum_{\vec{k}} I(\vec{k}) - I_{exp}(\vec{k}) \log I(\vec{k}) + \log \left(I_{exp}(\vec{k})! \right)$$

$$\mathcal{L}(I) \approx \sum_{\vec{k}} I(\vec{k}) - I_{exp}(\vec{k}) \left(\log I(\vec{k}) - \log I_{exp}(\vec{k}) + 1 \right)$$

where at the last step Stirling's approximation has been applied. In practice, a small offset ϵ must be added to prevent divergences inside the logarithms. This epsilon can be rationalized as a minimum signal recognizable by the detector. Signals significantly below this value are assumed to be corrupted by Gaussian noise. When counts are moderate, a variance stabilizing transform can be applied to Poisson distributed data to be approximately Gaussian with a constant variance, allowing the use of a least-squares estimator. This leads to the amplitude and Anscombe noise models. Given a transformation $x \mapsto 2\sqrt{x+c}$, the transformed variable can be modeled as Gaussian with unit variance. Once transformed, the Gaussian likelihood can be used:

$$\mathcal{L}(I) = \sum_{\vec{k}} \frac{1}{2} \left(\sqrt{I(\vec{k})+c} - \sqrt{I_{exp}(\vec{k})+c} \right)^2$$

$c = 0$ leads to the amplitude noise model, while $c = 3/8$ leads to the Anscombe noise model. The amplitude and Anscombe noise models have the benefit that additive Gaussian noise can be considered analytically, as discussed by Godard *et al.* [25].

For the conventional engines, gradients of the loss functions are taken analytically:

$$\nabla \mathcal{L}_p(\Psi) = \left(1 - \frac{I_{exp}(\vec{k})}{\epsilon + I(\vec{k})} \right) \psi(\vec{k})$$

$$\nabla \mathcal{L}_a(\Psi) = \left(1 - \frac{\sqrt{I_{exp}(\vec{k})+c}}{\epsilon + \sqrt{I(\vec{k})+c}} \right) \Psi(\vec{k})$$

As noted by Leidl *et al.* [60], these two gradients show significant differences in their spatial extent, with the Poisson gradient providing the largest updates at large scattering angles (where signals are weak).

Using these gradients, an optimal step size can be calculated [24], and a total wavefunction update can be found as $\Delta\Psi(\vec{k}) = -\alpha\nabla\mathcal{L}(\Psi)$. For instance, for the amplitude/Anscombe loss function:

$$\Delta\Psi(\vec{k}) = \frac{\sqrt{I_{exp}(\vec{k})+c}}{\epsilon + \sqrt{I(\vec{k})+c}} \Psi(\vec{k}) - \Psi(\vec{k})$$

In the amplitude noise model, this corresponds to the classic modulus constraint of the ePIE method [24].

B. Gradient descent solver

The gradient descent engine employs traditional machine learning algorithms to fit the system to the experimental data, minimizing the loss function \mathcal{L} , which consists of the loss on the detector plus the loss of each cost regularizer (described in the regularizers section). Autodifferentiation is used to efficiently obtain the local gradient $\nabla\mathcal{L}$ of the loss with respect to each optimization variable (known as the vector-Jacobian product). Since the loss function \mathcal{L} is a non-constant real function, it is not holomorphic. However, Wirtinger derivatives can be used [28] to overcome this challenge. For real functions, the two Wirtinger derivatives are equivalent up to a conjugation:

$$\overline{\frac{\partial f}{\partial z}} = \frac{\partial f}{\partial \bar{z}}$$

And the gradient $\mathbb{R} \rightarrow \mathbb{C}$ can be taken as:

$$\nabla\mathcal{L} = \overline{\frac{\partial\mathcal{L}}{\partial z}}$$

One of several optimizers may be used to perform the final update step for each variable. The Optax library [61] implements a number of gradient processing and optimization algorithms, including stochastic gradient descent (SGD), Adam and its variants [62, 63]. We are also interested in limited-memory Broyden-Fletcher-Goldfarb-Shanno (LBFGS) optimization and stochastic gradient descent with Polyak-Ribere step size [64]. Optimizer hyperparameters may be scheduled to vary as the reconstruction progresses, using set schedules (e.g cosine decay) or arbitrary Python expressions. We have found the Adam optimizer with a fixed learning rate to provide acceptable reconstructions in most cases. However, other optimization methods may allow significantly faster convergence or the reconstruction of difficult datasets.

C. Conventional solvers

Along with the gradient descent engine, **phaser** implements two conventional ptychography algorithms, ePIE and LSQML. The key difference between the gradient descent engine and the conventional engines is that, in the context of multislice ptychography, the conventional engines form an estimate of the optimized wavefront Ψ at the detector and on each layer. This optimized Ψ is used while calculating the gradient of the previous step. In contrast, in the gradient descent engine, the gradients are all taken simultaneously, and a step is taken in the direction of the gradient.

1. ePIE

In the ePIE algorithm, the noise model is first used to compute a wavefront update $\chi(\vec{k})$ on the detector. This update is propagated backwards to the exit plane of the sample. Then, at each slice, the wavefront update is split into an update applied to the object slice O_i , and to the previous wavefront/probe Ψ_i :

$$\begin{aligned}\chi_n(\vec{r}) &= \mathcal{F}^{-1}(\chi(\vec{k})) \\ \chi_{i-1} &= \frac{O_i^*(\vec{r})}{\max_{\vec{r}} |O_i(\vec{r})|^2} \chi_i(\vec{r}) \\ \Delta O_i &= \frac{P_i^*(\vec{r})}{\max_{\vec{r}} |\Psi_i(\vec{r})|^2} \chi_i(\vec{r})\end{aligned}$$

Probe updates are averaged across the group/batch of positions, while object updates are summed across the group (as well as incoherent probe modes):

$$\begin{aligned}P(\vec{r}) &+= \beta_{probe} \frac{\sum_k \chi_{0,k}(\vec{r})}{N_k} \\ O_i(\vec{r}) &+= \beta_{object} \sum_k \Delta O_{i,k}(\vec{r})\end{aligned}$$

This multislice generalization of ePIE (sometimes called 3PIE) was introduced by Maiden *et al.* [18] and is further discussed by Tsai *et al.* [19]. One can recognize $O^*(\vec{r})$ as the Wirtinger derivative $\frac{\partial}{\partial \bar{z}}$ of PO with respect to P , showing that single-slice ePIE can be considered a gradient descent method. For multislice, 3PIE diverges from pure gradient descent in that an update step is taken each slice, prior to the backpropagation of gradients to the previous slice.

2. LSQML

The multislice LSQML algorithm is implemented as described in Odstrčil *et al.* [24] and Tsai *et al.* [19]. Starting with the wavefront update in realspace $\chi_{n,k}(\vec{r})$, we first compute the illumination and object update directions using the steepest descent [24, eq 24]:

$$\begin{aligned}\Delta P_{i,k}(\vec{r}) &= \chi_{i,k}(\vec{r}) O^*(\vec{r}) \\ \Delta O_{i,k}(\vec{r}) &= \chi_{i,k}(\vec{r}) P^*(\vec{r})\end{aligned}$$

The illumination update direction $\Delta P_{i,k}$ is backwards-propagated and serves as the wavefront update $\chi_{i-1,k}$ for the previous slice. The object update direction is averaged across probe modes and group, and the step size is calculated per-group [24, eq 23,25]:

$$\begin{aligned}\Delta \hat{O}_i &= \frac{\sum_{group} \Delta O_{i,k}(\vec{r})}{\sum_{iter,k} |P_{i,k}(\vec{r})|^2 + \delta_O} \\ \alpha_{O,i} &= \frac{\sum_{\vec{r},k} \text{Re} [\chi_{i,k}(\vec{r}) (\Delta O_{i,k}(\vec{r}) P_{i,k}(\vec{r}))^*]}{\sum_{\vec{r},k} |\Delta O_{i,k}(\vec{r}) P_{i,k}(\vec{r})|^2 + \gamma}\end{aligned}$$

The final slice update is calculated as [24, eq 27]:

$$O_i(\vec{r}) += \beta_{object} \frac{\sum_{group} \alpha_{O,i} \Delta \hat{O}_i(\vec{r}) \sum_k |P_{i,k}(\vec{r})|^2}{\sum_{group,k} |P_{i,k}(\vec{r})|^2}$$

At the last slice, the probe update is calculated per-mode, analogously to the object. The intensity sums $\sum_{iter} |P_{i,k}(\vec{r})|^2$ and $\sum_{iter} \prod_i |O_{i,k}(\vec{r})|^2$ are computed progressively, with the final sum from iteration $i-1$ serving as the value for iteration i . The summed object intensity is recorded in the probe/cutout view, and encodes how transparent the object is to a given region of the probe. The summed probe intensity is recorded in the object view, and encodes how well illuminated a given region of the object is. The regularization parameters δ_P and δ_O are referred to as `illum_reg_probe` and `illum_reg_object` respectively.

D. Regularization

As ptychography is an ill-posed problem, regularizations help to stabilize the most likely solution, especially in the presence of noise. Regularizations act to either constrain the solution set to a desired subspace or to penalize unwanted features in the reconstruction, increasing convexity and prioritizing physically realistic solutions. The most critical regularization is the maximum likelihood noise model, which has been described above. However, in ptychography several other regularizations have been explored. For example, total variation (TV) regularization of the object phase has been shown to aid reconstructions in low-dose imaging [65].

`phaser` implements two main types of regularization. The first, known as constraint regularizations, are called per group or per iteration to constrain the reconstruction to some suitable subset of possible reconstruction states. Constraint regularizations are supported by all reconstruction engines.

Key constraint regularizations implemented by `phaser` are listed below:

Object amplitude constraint: Limits the object amplitude to within a specified range. Avoids the ambiguity noted by Fannjiang [59] whereby a scaling of the object amplitude can be compensated by a scaling of the illumination (or another object slice).

Probe support constraint: Limits the probe to a certain support in reciprocal or real space. Support constraints are widely used in phase retrieval [66, 67]

Layer regularization: Applies a Gaussian blur to the object in the depth axis. This blur is implemented with a real-space convolution to avoid information

bleeding from the top of the reconstructed object to the bottom.

Object low pass: Applies a Gaussian low pass filter to the object in the plane.

Object phase deramp: Removes an affine phase ramp from the object, one of the inherent ambiguities of ptychography [59].

The second type of regularization, known as cost regularizations, are added onto the detector loss in the gradient descent engine. These regularizations act to penalize physically unrealistic solutions and to suppress noise in the reconstruction.

Key cost regularizations implemented by **phaser** are listed below:

L2 regularization: (object, probe) L2 regularization (also known as ridge regression) acts to penalize excessive ‘energy’ in a signal; in this case it penalizes a nonzero probe intensity or a non-vacuum object.

L1 regularization: (object, object phase, object power spectrum) L1 regularization acts similarly to L2 regularization, but tends towards sparsity. This has been applied to the object power spectrum to bias the reconstruction towards periodic solutions [34].

Tikhonov regularization: (object, probe phase plate) Tikhonov regularization is applied to a finite difference operator, penalizing high frequency variation in the object or probe phase. This has the tradeoff of blurring the resulting image.

TV regularization: (object, probe phase plate) Similar to Tikhonov regularization, but enforces sparsity of the spatial derivative. Tends to create blocky, step-like features. Has been shown to improve reconstructions in low dose conditions [65].

Tikhonov/TV layer regularization: Tikhonov regularization applied in the depth direction of the object. The cost regularization equivalent of the ‘layers’ constraint regularization. TV regularization may be useful in cases where the object may change suddenly in depth (e.g a boundary or phase transition).

IV. Results

Two factors are important for performance of a ptychography package: Speed of reconstruction, including the speed of each iteration as well as the number of iterations required for convergence, and the final quality of reconstructions. Both are analyzed here.

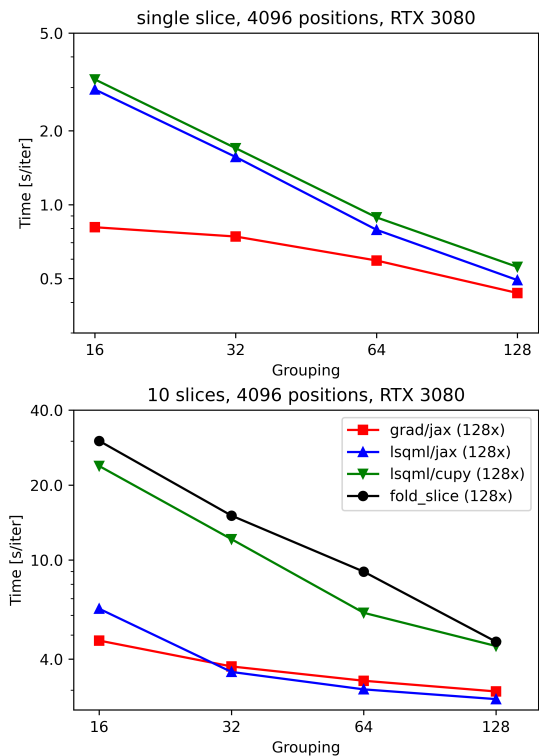


Figure 5. Reconstruction speed (measured as seconds per iteration) for a (top) single-slice and (bottom) multislice dataset of 4096 128x128 diffraction patterns reconstructed with multiple engines and computational backends (Red: Gradient descent engine with the JAX backend, Blue: LSQML engine with the JAX backend, Green: LSQML engine with the `cupy` backend, and Black: LSQML engine with the `fold_slice` fork of PtychoShelves). Smaller values indicate faster reconstructions.

Iteration speed is plotted as a function of ‘grouping’, which is how many probe positions are simulated simultaneously. Speed is shown for two representative datasets, one single slice dataset and one multislice (with 20 slices). Each dataset consists of a 64x64 scan (4096 total probe positions). Speed is plotted for the gradient descent engine with the JAX backend, and the LSQML engine with both the JAX and `cupy` computational backends. As a reference, the performance of the `fold_slice` fork of PtychoShelves [36] is plotted as well. In each condition, speed is measured with both 128x128 pixel diffraction patterns (solid line) and 192x192 pixel diffraction patterns (dashed line). All benchmarks were performed using a Nvidia RTX 3080 GPU running on an Ubuntu virtual machine. Performance depends heavily on grouping; large groupings are the fastest, at the expense of GPU memory. At small groupings, more time is spent in the relatively-slow Python interpreter. Grouping also affects convergence behavior, with larger groupings leading to more averaging of the update steps. All engines demonstrate improved performance compared to `fold_slice`. The greatest improvements are found for the JAX backend, which reaches iteration

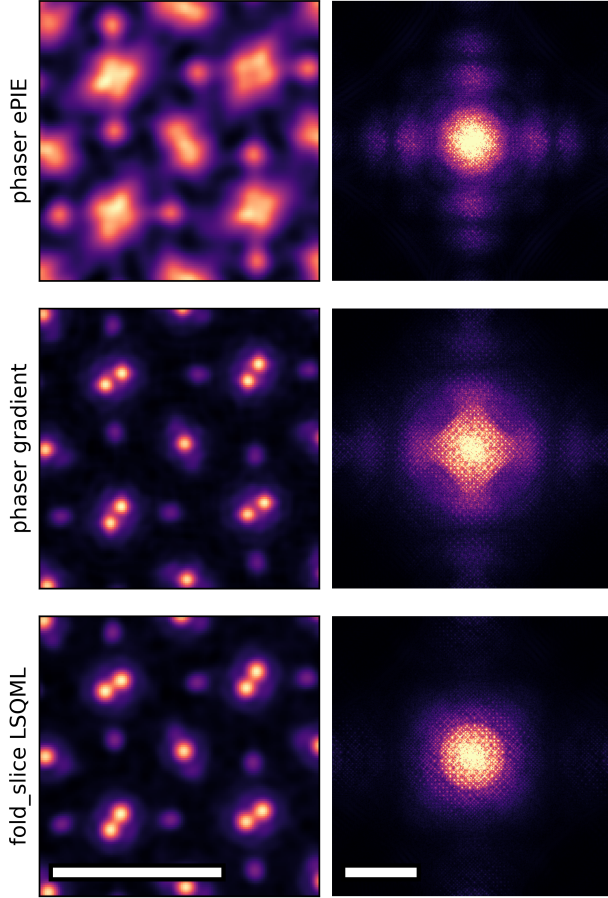


Figure 6. Comparison of PrScO₃ dataset [3] reconstructed with `phaser`'s ePIE and gradient descent engine, as well as `fold_slice`'s implementation of LSQML. The left column displays reconstructed object mean phase, while the right column displays the frequency spectrum (with a gamma of 0.2). Both LSQML and gradient descent provide superior performance to ePIE. Gradient descent provides information transfer to higher frequencies than LSQML, but the power spectrum is significantly anisotropic. Left scalebar 5 Å, right scalebar 5 Å⁻¹

times of less than 3 s/iter for a multislice dataset. This speed is in part due to JAX's just-in-time (JIT) engine, which compiles an optimized GPU kernel for each algorithm. In Ptychography, the bottleneck is the code that runs per group of probe positions, as this code is executed hundreds or thousands of times per iteration. In `phaser` with the JAX backend, this entire inner loop is JIT-compiled, leading to minimal time spent in the relatively slow Python interpreter. These improvements are most stark at small groupings, where the JAX backend outperforms both the `cupy` backend and `fold_slice` by a factor of 5-6x.

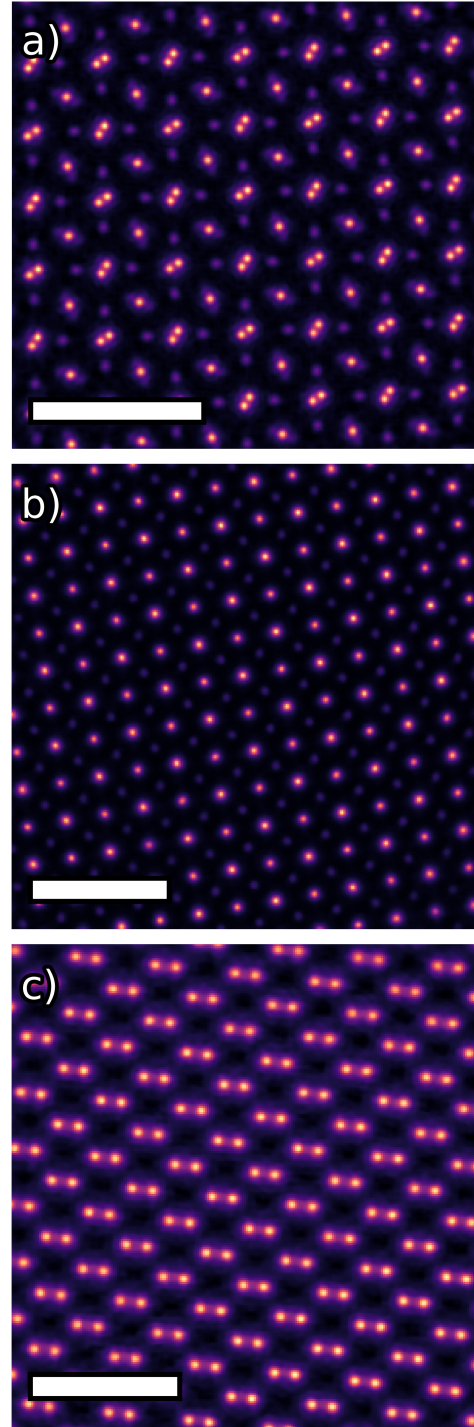


Figure 7. Example experimental reconstructions with the gradient descent engine of `phaser`. Scalebars 1 nm. a) PrScO₃ dataset from Ref. [3]. b) BaTiO₃ dataset. c) Si dataset from Ref. [44].

The final quality of reconstructions is showed for a PrScO₃ dataset [3] reconstructed with different engines in fig. 6. Both LSQML and gradient descent perform significantly better than ePIE for multislice datasets. Gradient descent provides slightly

better separation of the Pr-Pr dumbbells, as well as information transfer to higher frequencies. However, the gradient descent engine displays an anisotropic power spectrum, potentially complicating analysis of the reconstructed data. Representative experimental reconstructions performed with **phaser** are displayed in fig. 7. Reconstructions were performed with the gradient descent engine and the Poisson noise model. In practice, we find the gradient descent engine to be exceptionally robust to experimental data with both light and heavy elements.

V. Conclusions

phaser provides a common, declarative interface for multiple ptychographic reconstructions reconstruction engines and computational backends—enabling flexibility while retaining ease of use. **phaser** is designed to support multislice ptychography and incoherent probe modes, features which are critical for electron ptychography of materials. Web, notebook, and command line interfaces are provided, allowing **phaser** to scale from a single computer to the cloud and enabling the live viewing of in-progress reconstructions. **phaser** is released under the MPL 2.0 open-source license, and is available on GitHub at <https://github.com/hexane360/phaser> and the Python package interface (PyPI) as **phaserEM**.

VI. Acknowledgments

The authors thank Dr. Jingrui Wei for providing the BaTiO₃ experimental dataset. The authors acknowledge support from the Department of Homeland Security Countering Weapons of Mass Destruction Office (22CWDARI00046-01-00). This support does not constitute an express or implied endorsement on the part of the Government. This work was performed with the assistance of MIT SuperCloud.

References

- [1] Y. Jiang, Z. Chen, Y. Han, *et al.*, *Nature* **559**, 343 (2018).
- [2] Z. Chen, M. Odstrcil, Y. Jiang, *et al.*, *Nature Communications* **11**, 2994 (2020).
- [3] Z. Chen, Y. Jiang, Y.-T. Shao, *et al.*, *Science* **372**, 826 (2021).
- [4] H. Sha, J. Cui, and R. Yu, *Science Advances* **8**, eabn2275 (2022).
- [5] H. Sha, J. Cui, J. Li, *et al.*, *Science Advances* **9**, eadf1151 (2023).
- [6] Z. Chen, Y.-T. Shao, Y. Jiang, and D. Muller, *Microscopy and Microanalysis* **27**, 2146 (2021).
- [7] C. Gilgenbach, X. Chen, M. Xu, and J. LeBeau, *Microscopy and Microanalysis* **29**, 286 (2023).
- [8] J. Kim, K. Gordiz, D. Vivona, *et al.*, *ACS Nano* **18**, 31234 (2024).
- [9] Z. Dong, M. Huo, J. Li, *et al.*, *Nature* **630**, 847 (2024).
- [10] M. Zhu, M. Xu, Y. Yun, *et al.*, *ACS Nano* **19**, 5568 (2025).
- [11] J. M. Rodenburg and R. H. T. Bates, *Philosophical Transactions of the Royal Society of London. Series A: Physical and Engineering Sciences* **339**, 521 (1992).
- [12] J. M. Rodenburg and H. M. L. Faulkner, *Applied Physics Letters* **85**, 4795 (2004).
- [13] A. M. Maiden and J. M. Rodenburg, *Ultramicroscopy* **109**, 1256 (2009).
- [14] J. M. Rodenburg, A. C. Hurst, A. G. Cullis, *et al.*, *Physical Review Letters* **98**, 034801 (2007).
- [15] M. Humphry, B. Kraus, A. Hurst, *et al.*, *Nature Communications* **3**, 730 (2012).
- [16] A. J. D’Alfonso, A. J. Morgan, A. W. C. Yan, *et al.*, *Physical Review B* **89**, 064101 (2014).
- [17] P. Wang, F. Zhang, S. Gao, *et al.*, *Scientific Reports* **7**, 2857 (2017).
- [18] A. M. Maiden, M. J. Humphry, and J. M. Rodenburg, *Journal of the Optical Society of America A* **29**, 1606 (2012).
- [19] E. H. R. Tsai, I. Usov, A. Diaz, *et al.*, *Optics Express* **24**, 29089 (2016).
- [20] J. M. Cowley, A. F. Moodie, and IUCr, *The scattering of electrons by atoms and crystals. I. A new theoretical approach* (1957).
- [21] P. Thibault and A. Menzel, *Nature* **494**, 68 (2013).
- [22] C. Dwyer, R. Erni, and J. Etheridge, *Ultramicroscopy Proceedings of the International Workshop on Enhanced Data Generated by Electrons*, **110**, 952 (2010).
- [23] P. Thibault and M. Guizar-Sicairos, *New Journal of Physics* **14**, 063004 (2012).
- [24] M. Odstrčil, A. Menzel, and M. Guizar-Sicairos, *Optics Express* **26**, 3108 (2018).
- [25] P. Godard, M. Allain, V. Chamard, and J. Rodenburg, *Optics Express* **20**, 25914 (2012).
- [26] K. Giewekemeyer, P. Thibault, S. Kalbfleisch, *et al.*, *Proceedings of the National Academy of Sciences* **107**, 529 (2010).
- [27] P. Thibault, M. Dierolf, O. Bunk, *et al.*, *Ultramicroscopy* **109**, 338 (2009).
- [28] E. J. Candès, X. Li, and M. Soltanolkotabi, *IEEE Transactions on Information Theory* **61**, 1985 (2015).
- [29] Y. S. G. Nashed, T. Peterka, J. Deng, and C. Jacobsen, *Procedia Computer Science International Conference on Computational Science, ICCS 2017, 12-14 June 2017, Zurich, Switzerland*, **108**, 404 (2017).
- [30] S. Kandel, S. Maddali, M. Allain, *et al.*, *Optics Express* **27**, 18653 (2019).
- [31] M. Schloz, T. C. Pekin, Z. Chen, *et al.*, *Optics Express* **28**, 28306 (2020).
- [32] M. Du, S. Kandel, J. Deng, *et al.*, *Optics Express* **29**, 10000 (2021).
- [33] J. Seifert, D. Bouchet, L. Loetgering, and A. P. Mosk, *OSA Continuum* **4**, 121 (2021).
- [34] B. Diederichs, Z. Herdegen, A. Strauch, *et al.*, *Nature Communications* **15**, 101 (2024).
- [35] B. Enders and P. Thibault, *Proceedings of the Royal Society A: Mathematical, Physical and Engineering Sciences* **472**, 20160640 (2016).
- [36] K. Wakonig, H.-C. Stadler, M. Odstrčil, *et al.*, *Journal of Applied Crystallography* **53**, 574 (2020).
- [37] L. Loetgering, M. Du, D. B. Flaes, *et al.*, *Optics Express* **31**, 13763 (2023).
- [38] C.-H. Lee, S. E. Zeltmann, D. Yoon, *et al.*, *PtyRAD: A High-performance and Flexible Ptychographic Reconstruction Framework with Automatic*

- Differentiation (2025).
- [39] Q. Meng, W. Chen, Y. Wang, *et al.*, *Neurocomputing* **337**, 46 (2019).
- [40] J. Bradbury, R. Frostig, P. Hawkins, *et al.*, JAX: composable transformations of Python+ NumPy programs (2018).
- [41] X. Qian and D. Klabjan, The Impact of the Mini-batch Size on the Variance of Gradients in Stochastic Gradient Descent (2020).
- [42] F. Mignacco, P. Urbani, and L. Zdeborová, *Machine Learning: Science and Technology* **2**, 035029 (2021).
- [43] T. B. Edo, D. J. Batey, A. M. Maiden, *et al.*, *Physical Review A* **87**, 053850 (2013).
- [44] C. Gilgenbach, X. Chen, and J. M. LeBeau, *Microscopy and Microanalysis*, ozae055 (2024).
- [45] R. Skoupy, D. G. Stroppa, M. Guizar-Sicairos, *et al.*, *Microscopy and Microanalysis* **30**, ozae044.913 (2024).
- [46] J. M. LeBeau, S. D. Findlay, L. J. Allen, and S. Stemmer, *Ultramicroscopy* **110**, 118 (2010).
- [47] M. C. Cao, Z. Chen, Y. Jiang, and Y. Han, *Scientific Reports* **12**, 12284 (2022).
- [48] T. Akiba, S. Sano, T. Yanase, *et al.*, Optuna: A Next-generation Hyperparameter Optimization Framework (2019).
- [49] J. Bergstra, R. Bardenet, Y. Bengio, and B. Kégl, in *Advances in Neural Information Processing Systems*, Vol. 24 (Curran Associates, Inc., 2011).
- [50] R. Dosselmann and X. D. Yang, *Signal, Image and Video Processing* **5**, 81 (2011).
- [51] J. Nilsson and T. Akenine-Möller, Understanding SSIM (2020).
- [52] E. J. Verbeke, M. A. Gilles, T. Bendory, and A. Singer, *Communications Biology* **7**, 101 (2024).
- [53] C. R. Harris, K. J. Millman, S. J. van der Walt, *et al.*, *Nature* **585**, 357 (2020).
- [54] R. Okuta, Y. Unno, D. Nishino, *et al.*, in *Proceedings of Workshop on Machine Learning Systems (LearningSys) in The Thirty-first Annual Conference on Neural Information Processing Systems (NIPS)* (2017).
- [55] H. Park, J. H. Lee, Y. Oh, *et al.*, Training Deep Neural Network in Limited Precision (2018).
- [56] A. Kuzmin, M. V. Baalen, Y. Ren, *et al.*, FP8 Quantization: The Power of the Exponent (2024).
- [57] S. Venkataramani, V. Srinivasan, W. Wang, *et al.*, in *2021 ACM/IEEE 48th Annual International Symposium on Computer Architecture (ISCA)* (2021) pp. 153–166.
- [58] E. J. Kirkland, *Advanced Computing in Electron Microscopy* (Springer US, Boston, MA, 2010).
- [59] A. Fannjiang, *Multiscale Modeling & Simulation* **17**, 973 (2019).
- [60] M. L. Leidl, B. Diederichs, C. Sachse, and K. Müller-Caspary, *Micron* **185**, 103688 (2024).
- [61] DeepMind, I. Babuschkin, K. Baumli, *et al.*, The DeepMind JAX Ecosystem (2020).
- [62] D. P. Kingma and J. Ba, Adam: A Method for Stochastic Optimization (2017).
- [63] T. Dozat, in *ICLR 2016* (San Juan, Puerto Rico, 2016).
- [64] N. Loizou, S. Vaswani, I. H. Laradji, and S. Lacoste-Julien, in *Proceedings of The 24th International Conference on Artificial Intelligence and Statistics* (PMLR, 2021) pp. 1306–1314.
- [65] M. Tanksalvala, C. L. Porter, Y. Esashi, *et al.*, *Science Advances* **7**, eabd9667 (2021).
- [66] J. R. Fienup, *Applied Optics* **21**, 2758 (1982).
- [67] V. Elser, *JOSA A* **20**, 40 (2003).